
ISAS-NASA GEOTAIL Satellite (1992)

A. Nishida and Toshifumi Mukai

Contents

Introduction	372
Spacecraft, Scientific Payload, and Orbit	373
Basic Structure of the Magnetotail	377
Near-Earth Reconnection and Substorm	378
Structure of the Reconnection Region	385
Sources of Magnetotail Plasma	388
Solar Wind Entry Following Magnetic Reconnection on the Dayside	
Magnetopause	389
Solar Wind Entry from the Flanks of the Tail	390
Plasma of the Terrestrial Origin	391
Waves in the Magnetotail	393
Conclusion	394
References	395

Abstract

GEOTAIL spacecraft launched on 24 July 1992 has explored the Earth's magnetotail across the range of 10–210 R_E from the Earth. GEOTAIL not only clarified the basic structure of the magnetotail both in quiet and active times, but it also revealed the kinetics of the plasma that underlies macroscopic dynamics. In the magnetotail magnetic reconnection is the key process which governs energy dissipation and acceleration of ions and electrons. GEOTAIL has

A. Nishida and T. Mukai are retired

A. Nishida (✉)

Institute of Space and Astronautical Science, Machida, Tokyo, Japan

e-mail: hirosoph@dj.mbn.or.jp

T. Mukai

Institute of Space and Astronautical Science, Japan Aerospace Exploration Agency,
Hino, Tokyo, Japan

e-mail: t-mukai@mail.hinocatv.ne.jp; mukai@stp.isas.jaxa.jp

addressed the relation between the reconnection and auroral phenomena and clarified the kinetics of the energy conversion process in the reconnection region that operates on the scale of the ion inertia length. Understandings have also been advanced on the entry of the solar wind plasma into the magnetotail due to turbulence generated on the magnetopause and the excitation of plasma waves on account of prevalent nonequilibrium velocity distributions of plasma particles. The processes addressed by *in-situ* observations by GEOTAIL in space should be common to collisionless plasmas that prevail in astrophysical objects.

Keywords

Magnetotail • Plasma sheet • Plasmoid • Lobe • Solar wind • Aurora • Substorm • Acceleration • Heating • Reconnection • Neutral line • Convection • Kelvin-Helmholtz instability • Hall current • Ion-electron decoupling

Introduction

Cosmic rays, that is, energetic ions and electrons having energies up to $\sim 10^{21}$ erg, pose the greatest threat to life in the universe. However, the life on the Earth has been protected from the most part of the spectrum by the magnetic field generated by the dynamo action in the core region. Under the pressure of the solar wind that flows continually from the solar corona, the geomagnetic field is enclosed in a domain called magnetosphere which shields much of the cosmic rays. The magnetosphere is not quiet and static. Solar wind produces a complex structure and activates the magnetosphere. This is the subject of this chapter.

Energy and momentum imparted from the solar wind generate global convection in the magnetosphere which circulates between the day and the night side. Geomagnetic field lines are stretched at the same time and form the magnetotail extending behind the Earth. The magnetic energy is converted to the kinetic energy in the magnetotail. This energy conversion occurs primarily through the magnetic reconnection at the neutral sheet in the magnetotail. The collapse of extended field lines produces a variety of disturbances such as substorms on the earthward side of the reconnection region, while plasmoid is ejected on its anti-earthward side. Thus the magnetotail plays a key role in the dynamics of the magnetosphere.

The GEOTAIL spacecraft was uniquely designed to address the physics of the Earth's magnetotail. The prime target was the magnetic reconnection in the near-Earth magnetotail: its location and development, relation to substorms, and microscopic structure of the energy conversion process. Also studied are the solar wind entry into the magnetosphere, outflow of ionospheric ions to the magnetotail, and excitation of plasma waves in the tail plasma. These are the basic processes that make the foundation of the space weather phenomena.

GEOTAIL was implemented as a joint mission between ISAS (Institute of Space and Astronautical Science) of Japan and NASA of USA. ISAS developed the spacecraft and NASA launched it. Responsibilities for onboard instruments were

shared. It was launched on 24 July 1992 and has been working soundly for more than two solar cycles by now. Acquired data have been openly disseminated to the international space science community.

Spacecraft, Scientific Payload, and Orbit

The configuration of the GEOTAIL spacecraft is shown in Fig. 1. It has a cylindrical shape with diameter of 2.2 m and height of 1.6 m. Two masts with 6-m length are deployed symmetrically to separate the magnetometers from the main body, and four 50-m wire antennas are deployed to measure the electric field from DC to 800 kHz. Particular attention was paid to make the spacecraft electromagnetically clean. The spacecraft attitude is spin stabilized with the rate of 20 rpm and with the axis being nominally perpendicular to the ecliptic plane; more exactly, the spin axis was controlled to be inclined sunward and make an angle of 87° with respect to the solar ecliptic plane for 11.5 years after launch until the fuel was exhausted.

Seven sets of science instruments are on board GEOTAIL, as listed in Table 1. Measured items constitute basic elements of space plasmas. Magnetic field represents the framework of the magnetosphere. Electric field reflects the plasma dynamics. Waves in these fields are essential ingredients of the collisionless plasma. A unique feature in the plasma wave instrument is the waveform capture (WFC), which was

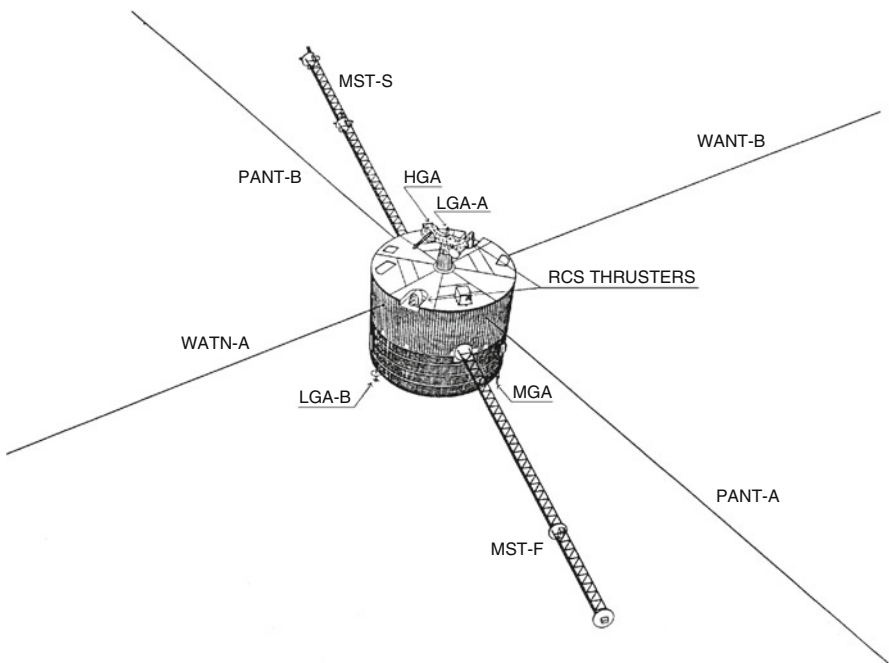


Fig. 1 Configuration of the GEOTAIL spacecraft (Nishida 1994)

Table 1 Science instruments on board GEOTAIL (Nishida 1994)

Item	Description	Range	PI*, co-I
Electric field (EFD)	Spherical probe and wire antenna	dc – 32 Hz (2 comp)	K. Tsuruda*
	Electron boomerang	dc – 10 Hz (3 comp)	F.S. Mozer
	Ion emitter		R. Schmidt
Magnetic field (MGF)	Fluxgate	dc – 16 Hz (3 comp)	S. Kokubun*
	Search coil	1–50 Hz (3 comp)	M. Acuna
			D.H. Fairfield
Plasma (LEP)	Ion/electron 3-dim.velocity distributions	10 eV–40 keV/q	T. Mukai*
	Solar wind ions	150 eV–8 keV/q	
	Ion mass/energy spectrum	0.1–25 keV/q	
Plasma (CPI)	Ion/electron 3-dim velocity distributions	1 eV–50 keV/q	L.A. Frank*
	Solar wind ions	150 eV–7 keV/q	
	Ion mass/energy spectrum	1 eV–50 keV/q	
Energetic particles (HEP)	Low-energy particles	30 keV–1.5 MeV/n	T. Doke*
	Ion/electron burst	0.7–3.5 MeV/n	B. Wilken
	Medium-energy ion isotope ratio	5–50 MeV/n	
	High-energy ion isotope ratio	10–230 MeV/n	
Energetic particles (EPIC)	Ion charge state/mass/energy	30–230 keV/q	D.J. Williams*
	Ion mass and energy	> 50 keV–5 MeV	
	Electron energy	> 30 keV	
Plasma waves (PWI)	Frequency sweep	E: 25 Hz–800 kHz	H. Matsumoto*
	Multichannel analyzer	H:25 Hz–12.5 kHz	R.R. Anderson
	Waveform capture	10 Hz–4 kHz	

quite a new technique in those days (although it has become common to plasma wave instruments on board recent spacecraft). Plasma and particles are measured by four sets of experiments because of their vital importance in physics of the magnetosphere. Energy ranges for the ion measurements covered by these experiments are shown in Fig. 2. For detailed description of each instrument, refer to the special section “GEOTAIL Instruments and Initial Results” of the *Journal of Geomagnetism and Geoelectricity* (vol. 46, pp. 3–95 and 669–733, 1994).

One of the plasma instruments, the low-energy plasma (LEP) experiment, became inoperative on 22 August 1992, when a latch-up occurred in the key part

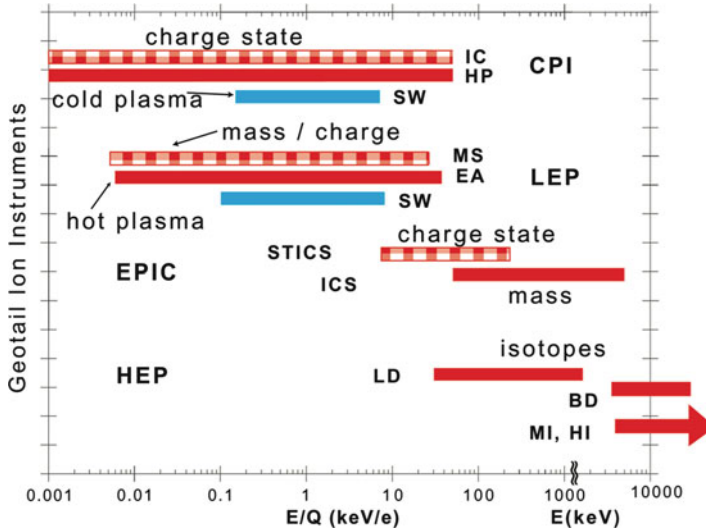


Fig. 2 Energy coverage of plasma and particle experiments on board GEOTAIL

of the electronic circuit due to electrical arcing, but this instrument was revived on 1 September 1993, by turning off the spacecraft power in the lunar shadow which was created on purpose. No experiments were adversely affected by this special operation. The recovery of LEP was critical for the success of the GEOTAIL mission, since most of the results to be described in the subsequent sections have been brought forth by the LEP observations.

A key feature of the LEP energy-per-charge analyzers is geometrical factors which are larger than the conventional ones in those days; the geometrical factor of the LEP ion analyzer is more than 20 times larger than that of the CPI hot plasma analyzer. The large geometrical factor of LEP means high sensitivity so that high time resolution measurements can be made with sufficient counting statistics. This has proved to be vital especially for the studies of magnetic reconnection and plasma transport processes across boundary layers (i.e., magnetopause as well as internal boundaries such as the plasma sheet boundary layer). On the other hand, the detection efficiency of micro-channel plates (MCP), the particle detectors used along with the energy analyzers, generally degrades with the total counts integrated over the measurements when they are operated with a fixed bias voltage. Therefore, the degradation would be faster if the count rate is higher. The bias voltage is increased if the detector gain of LEP decreases in order to keep the detection efficiency at a reasonable value. The degradation rate, however, was much slower than had been anticipated, and as of 2014 after more than 20 years have elapsed, the LEP instrument is still providing useful observations of magnetospheric plasma.

It is mandatory to calibrate the detection efficiency with in-flight data, since the efficiency varies with the instrument operation time. In LEP, the ion detectors are calibrated as follows. At first, after subtraction of background noise, relative

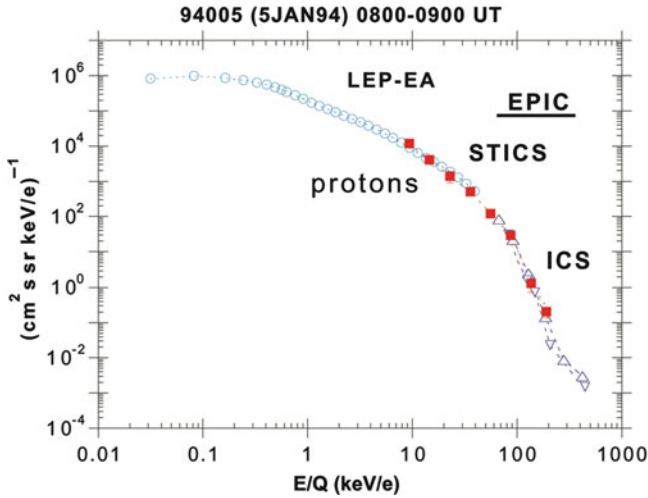


Fig. 3 Comparison of proton energy distributions measured by three different instruments, LEP-EA, EPIC-STICS, and EPIC-ICS, on board GEOTAIL (Courtesy of ISAS/JAXA)

efficiencies between different channels (detectors at different elevation angles) are examined. Fortunately the relative efficiencies of the ion detectors have not changed throughout the observation, so that those measured in the preflight calibration experiment in the laboratory have been used. Then, ion velocity moments are calculated, and the resultant ion density is compared with electron density estimated from the plasma wave data: cutoff frequency of the continuum radiation in various regions including plasma sheet, lobe, and magnetosheath. From this comparison, the absolute value of the ion detection efficiency can be obtained. Correction of the electron detection efficiency needs a more complicated procedure, since the electron data are sensitive to the spacecraft potential and contain spurious data due to photoelectrons and secondary electrons. In addition, the detector efficiency depends on the electron energy. The detail of the calibration method is described elsewhere (Saito and Mukai 2007; McFadden et al. 2007).

Figure 3 shows an example of proton energy distribution measured by three different instruments, LEP-EA, EPIC-STICS, and EPIC-ICS. Although calibrations of the three instruments were carried out independently, agreement among data of these instruments is excellent, which demonstrates high reliability of the respective calibration procedures.

For the first 2 years, the spacecraft surveyed the distant magnetotail (with apogees on the nightside at 80–210 R_E from the Earth) by executing double-lunar-swingbys orbits. The orbits in this distant-tail phase are shown in Fig. 4 (left) with xy projection on top and xz projection at bottom. The apogee was lowered to 50 R_E in mid-November 1994 and then further down to 30 R_E in order to focus on the magnetic reconnection in the near-Earth magnetotail. The inclination was set at -7° in order that the apogee is to be on the tail midplane, which is

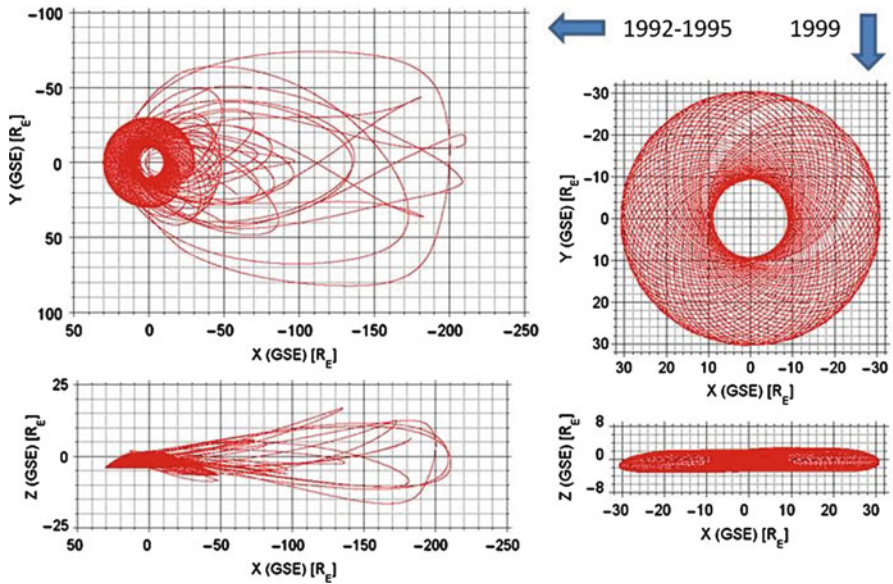


Fig. 4 Orbits of the GEOTAIL spacecraft (Courtesy of ISAS/JAXA)

hinged to the geomagnetic equatorial plane at about $10 R_E$ at midnight, around the December solstice when the spacecraft is free from shadowing by the Earth. The perigee was about $10 R_E$ so that the spacecraft skimmed the magnetopause on the dayside; it was further reduced later to $9-9.5 R_E$ to increase the chances of observing the low-latitude boundary layer of the magnetosphere. The orbits in 1999 are shown in Fig. 4 (right). After 2007 the orbit is no longer controlled and currently the inclination is about 30° .

Basic Structure of the Magnetotail

Figure 5 shows the noon-midnight meridional section of the magnetotail in quiet (a) and active (b) conditions (Hones 1984, modified). The x direction is toward the sun, the z direction contains the Earth’s magnetic dipole, and the y direction is perpendicular to x and z. Magnetic field is directed earthward in the northern half of the tail and anti-earthward in the southern half. The “tail lobe” in high latitudes is filled by open field lines which have only one root on the Earth. In low latitudes field lines are closed, that is, they have both roots on the Earth. The interface where the sunward component \mathbf{B}_x is zero is called the neutral sheet. Actually the neutral sheet is often inclined to the (x,y) plane. In the absence of the reconnection, \mathbf{B}_z should be northward everywhere.

However, magnetic field lines are reconnected in the magnetotail and hence \mathbf{B}_z is southward beyond certain distance. In quiet times the magnetic neutral line, where \mathbf{B}_z changes from northward to southward, is located in the distant tail (Fig. 5a).

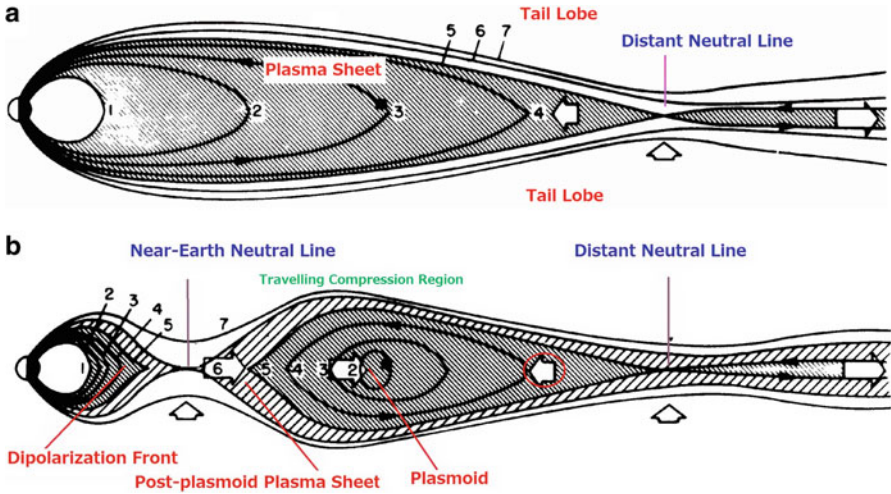


Fig. 5 Basic structure and terminology of the magnetotail in (a) quiet and (b) active states (After Hones (1984), modified)

This neutral line, called “distant neutral line,” marks the demarcation between the closed field lines and the open field lines. The open field lines have been produced by reconnection on the dayside magnetopause, move from the lobe region toward the neutral sheet, and are closed by reconnection at the distant neutral line. Plasma which has been heated in the process flows earthward on the earthward side of the neutral line and anti-earthward on the anti-earthward side. The earthward flow accompanies closed field lines, and the anti-earthward flow accompanies the field lines that are no longer rooted on the Earth and extended to the solar wind. The hot plasma deposited on the closed field lines constitutes the “plasma sheet.” Magnetic flux transported by the flow is represented by $E_y = V_x B_z$. To find the location of the distant neutral line, seven orbits of GEOTAIL are selected when the geomagnetic activity index K_p was higher than 3 for 24 h or more, and the sums of E_y are calculated separately for intervals of the tailward flow and the earthward flow. The ratio between them is plotted in Fig. 6. A sharp drop of the ratio is seen at a distance of about $130 R_E$ from the Earth, suggesting that the neutral line tends to be located around this distance in moderately active times (Nishida et al. 1996). This does not necessarily mean, however, that the distant neutral line stays at any fixed position, because it could be pushed tailward by the outflowing plasma from a new reconnection line produced later on the earthward side (Maezawa and Hori 1998).

Near-Earth Reconnection and Substorm

In active times another neutral line is formed in the near-Earth region (Fig. 5b) where field lines were formerly closed. Distance to the “near-Earth neutral line (NENL)” is in the x range of -20 to $-30 R_E$ (Nagai et al. 1998). The major factor

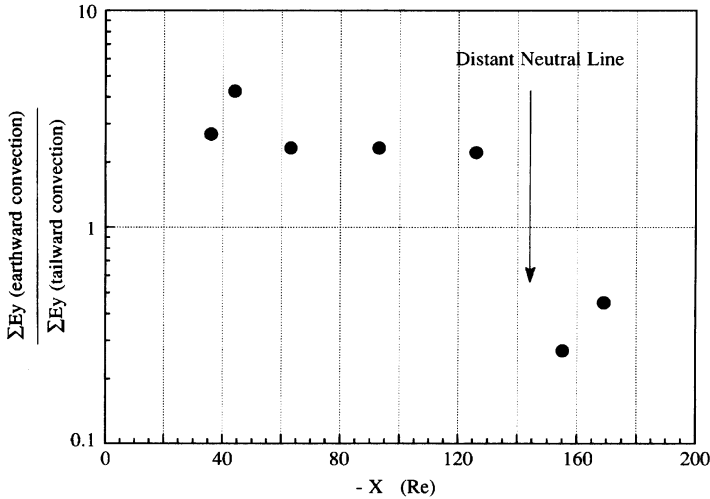


Fig. 6 Ratio between magnetic fluxes transported tailward and earthward is plotted against the distance x from the Earth. The drop of this ratio from >1 to <1 identifies the location of the magnetic neutral line (Nishida et al. 1996)

that determines the distance to NENL is the electric field in the solar wind given by $\mathbf{V}_{sw,x} \times \mathbf{B}_{sw,s}$ where $\mathbf{B}_{sw,s}$ is the southward component of the interplanetary magnetic field. Reconnection takes place closer to the Earth when this parameter is higher. The effect of the solar wind dynamic pressure is minor (Nagai et al. 2005).

Since closed field lines are reconnected at the NENL, a loop of field lines are produced on the anti-earthward side of the NENL. This is the “plasmoid.” Propagation of bulge-shaped plasmoid produces “Travelling Compression Region” on the lobe side. When all the closed field lines have been reconnected, the open field lines which were originally in the tail lobe are reconnected, and this results in field lines which have both ends extended to the interplanetary space. These field lines constitute “post-plasmoid plasma sheet.”

Plasmoid and post-plasmoid plasma sheet are observed as a time sequence when spacecraft is located on the anti-earthward side of the NENL. In the case shown in Fig. 7a (Ieda et al. 2001), three events were recorded in a row. The blue vertical lines mark passage of the center of the plasmoid where \mathbf{B}_z changed sign from northward to southward. Increase of the anti-earthward flow speed ($-\mathbf{V}_x$) had started a few minutes before each of them, suggesting that compressional wave from the advancing plasmoid had set the upstream plasma into motion. The fast tailward flow that lasts after $|\mathbf{B}_z|$ has returned to very small values corresponds to the post-plasmoid plasma sheet. (The earthward flow from the distant neutral line, which is circled by red in Fig. 5b, sometimes makes the plasmoid stagnant, but eventually it is pushed away when more energetic plasmoid is generated anew.)

A statistical study of plasmoids observed at x of -16 to $-210 R_E$ has shown the following features (Ieda et al. 1998). In the near-tail around $x = -30 R_E$, plasmoids

are accelerated and expanding in y direction. Typical size in the near-tail at $x = -30 R_E$ is $4 R_E$ (in x) \times $20 R_E$ (in y), and at $x = -190 R_E$ it has grown to $10 R_E$ (in x) \times $40 R_E$ (in y) \times $10 R_E$ (in z). Speed and temperature decrease with distance. The energy flux carried by each plasmoid is 10^{14} J around $x = -90 R_E$. The thermal component is the dominant contributor.

Images of aurora at the corresponding interval are shown in Fig. 7b. (Each panel covers the geomagnetic latitudes of $60\text{--}90^\circ$ and the sun is to the left.) These were taken on board the POLAR spacecraft, and the position of GEOTAIL is projected in the fifth panel; it was nearly on the midnight meridian. Auroral breakups, that is, brightening and expansion of the aurora, are seen in three panels whose times are

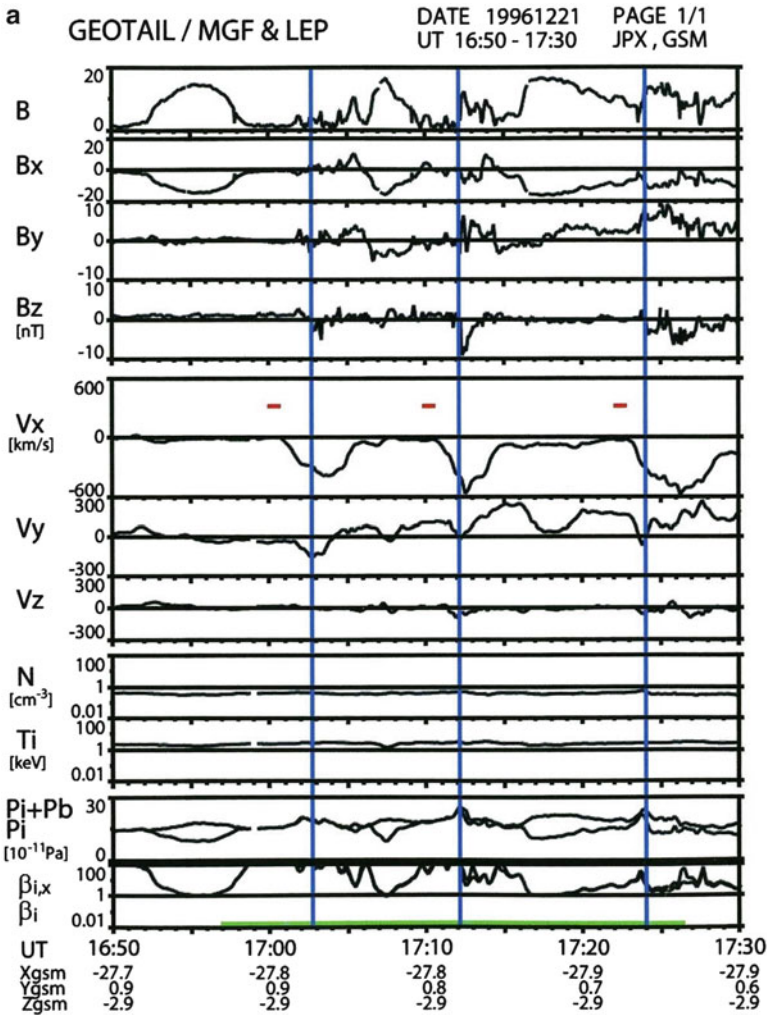


Fig. 7 (continued)

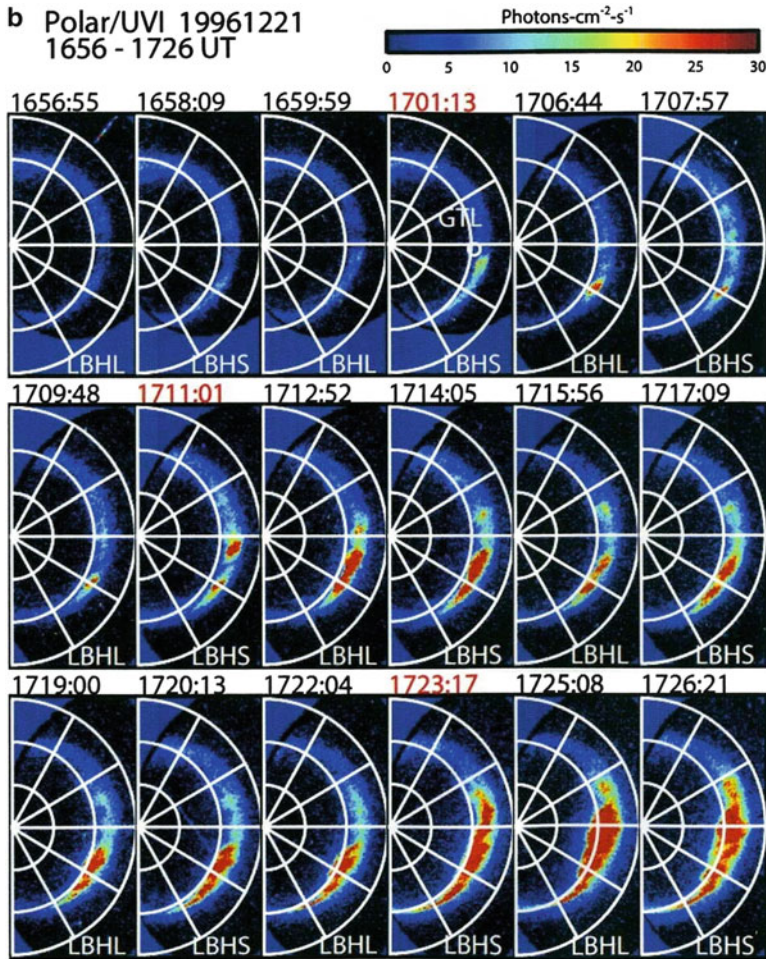


Fig. 7 Correspondence between (a) the reconnection signatures observed by GEOTAIL and (b) the auroral observation by POLAR (Ieda et al. 2001)

written in red, and these times are given by red bars above the V_x record of Fig. 7a. It can be seen that all of them occurred at the time of increases of the anti-earthward flow ahead of plasmoids. As seen in this example, auroral breakups are accompanied by fast tailward flows within the dawn-dusk width of $\sim 10 R_E$ of the LT meridian where breakup takes place (Ieda et al. 2008).

On the Earthward side of the Near-Earth Neutral Line, it is expected from Figure 5b that the earthward flow becomes stronger and the magnetic field lines become less stretched and more dipolar. Increases in V_x and B_z were indeed observed in the case shown in Figure 8 (obtained at $14 R_E$ and 2300 LT; Fairfield et al. 1999) when dramatic brightening of aurora took place between 06:22 and 06:28 images that span the time of the 06:27 flow burst (indicated by vertical dashed

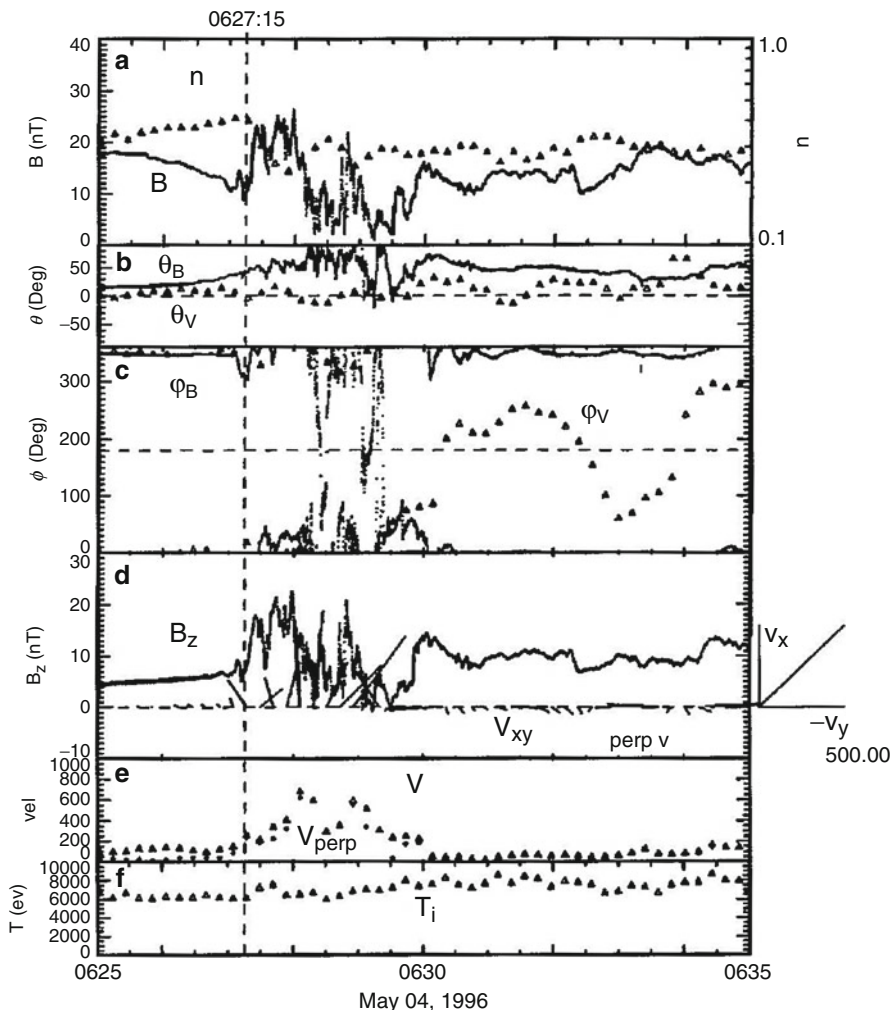


Fig. 8 Dipolarization and earthward flow observed on the earthward side of the neutral line (Fairfield et al. 1999)

line). But density n decreased at this time while the model of Figure 5b may suggest that the compressed plasma sheet plasma is driven earthward ahead of the low-density plasma introduced from the lobe.

The apparent contradiction can probably be overcome by the mechanism proposed by Pontius and Wolf (1990). The electric current that stretches the field lines in the tail is carried by diamagnetic drifts of ions across the tail. When a bubble of plasma having lower density than the ambient medium is injected, this current is partially blocked at dawn and dusk boundaries of the

bubble, and electric field is produced by polarization. This field is directed from dawn to dusk and adds to the electric field that drives convection globally throughout the magnetosphere. The location of the flows is centered about 0.4 h magnetic local time east of auroral expansion and is localized with a width of 3–5 R_E (Nakamura et al. 2001).

Dipolarization in the near-tail plasma sheet is followed by injection of energetic particles to the inner magnetosphere. This can be seen in Fig. 9 (Sergeev et al. 2000) where the data obtained by GEOTAIL at $x \sim -26 R_E$ (in four panels in the middle) are compared with the observations at the geosynchronous satellites LANL080 and LANL84 (in two bottom panels). (LANL stands for Los Alamos National Laboratory.) All these spacecraft were close to the magnetic midnight when these observations were made. The second dashed line (at 2023 UT) delineates arrival of the dipolarization front at GEOTAIL, which is signified by increase in earthward convection $\mathbf{V}_{x\perp}$, increase in \mathbf{B}_z , increase in $(\mathbf{V} \times \mathbf{B})_y$, and decrease in total and thermal pressures P_T and P_p . About 8 min after this, injection of ~ 100 keV electrons was observed by LANL080. The time delay implies the average propagation velocity of ~ 250 km/s. Another 3 min later, the injection was observed at LANL084 with energy dispersion which can be attributed to azimuthal magnetic drift from near the meridian of LANL080. The top panel of Fig. 9 is the record of the ion precipitation obtained by Interball-Auroral satellite at an altitude of $\sim 3 R_E$ in high latitude. The energy dispersion of the ions (between 2025 and 2031 UT) can be interpreted to be the time-of-flight effect of particles impulsively accelerated in the distant tail at about $40 R_E$. As for the aurora (whose records are not reproduced here), narrow streamer started to disintegrate in the poleward half at ~ 2022 UT, and signature of activation in the poleward oval could be discerned at ~ 2025 UT after which a wider streamer structure reappeared. This auroral feature can be attributed to the electron acceleration along the upward field-aligned current that flows from the duskside boundary of the polarized plasma bubble. Similar sequence of events was observed at another case in Fig. 9 delineated by the first dashed line.

The energy flow in the dipolarization region is shown in Fig. 10. Poynting flux in the lobe and PSBL (plasma sheet boundary layer) toward the plasma sheet is shown in top panels, and the thermal energy flux in the plasma sheet and PSBL toward the Earth is shown in bottom panels. Left and right panels correspond to two different ranges of x , -6 to $-12 R_E$ and -12 to $-20 R_E$, respectively. Records are shown for an interval of 20 min centered on the onset time (taken as $t = 0$) of the auroral breakup observed by POLAR or IMAGE satellite (Miyashita et al. 2012). Although the data points are much scattered, the averages seem to indicate that the parameters increased around $t = 0$. Increase in Poynting flux PF_z toward the PSBL (top panels) represents the flow of the lobe field lines that occurs when reconnection is in progress, and increase in the earthward component TF_x of the thermal energy flux in the plasma sheet represents the earthward flow of the heated ions from the direction of the neutral line region. The energy transported by PF_z to the plasma sheet amounts to $\sim 0.42\text{--}1.26 \times 10^{14}$ J.

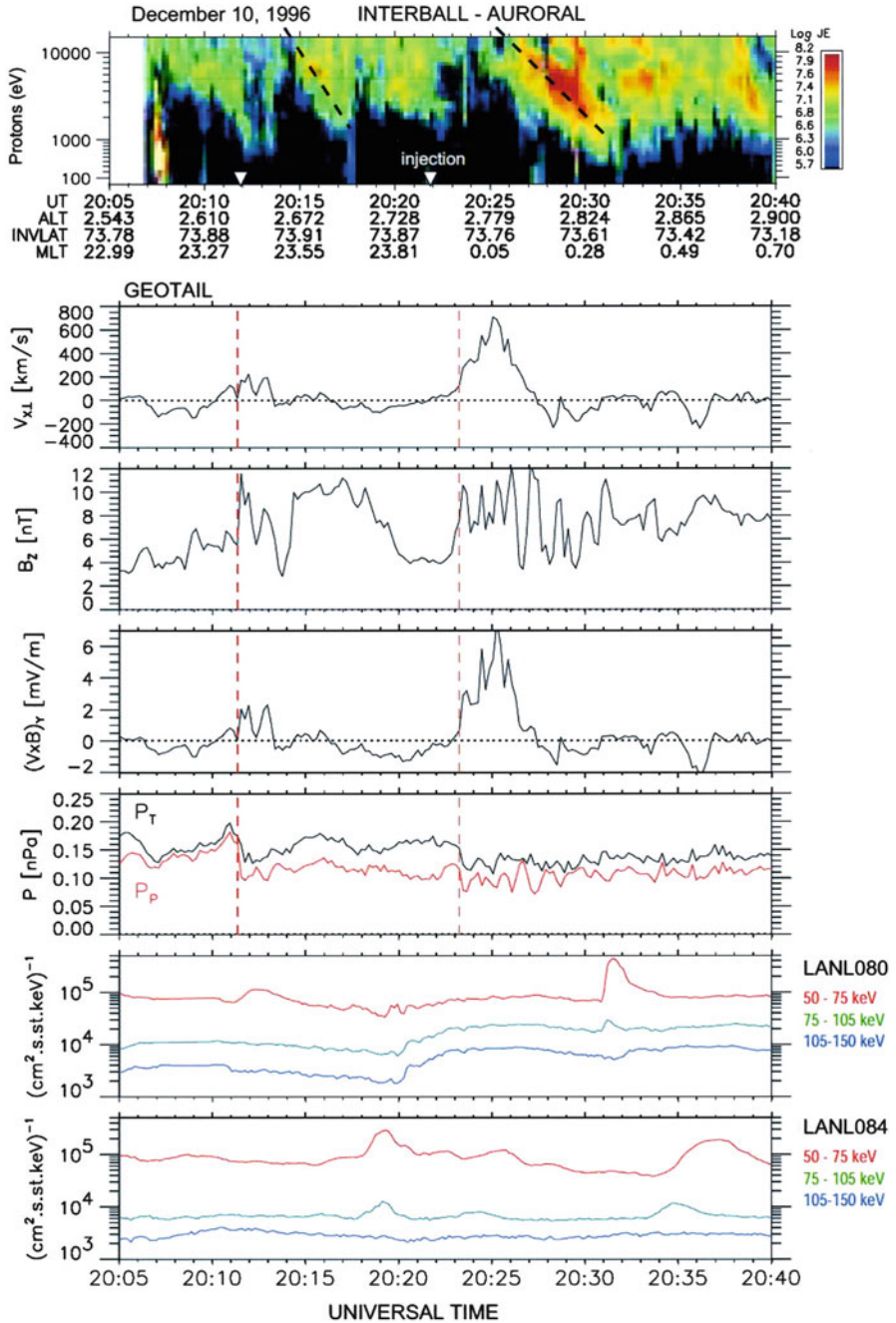
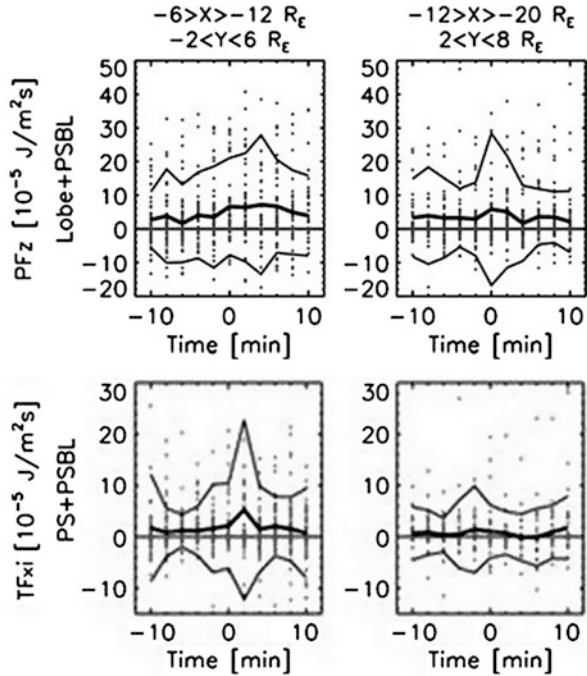


Fig. 9 Injection of energetic particles to the geosynchronous orbit at the time of dipolarization in the near-Earth plasma sheet (Sergeev et al. 2000)

Fig. 10 Energy flux in the dipolarization region (*left*) and in its tailward region (*right*). Z component of the Poynting flux (PF_z) is on *top* and x component of the thermal energy flux (TF_{xi}) is at *bottom*. Origin of the time is the auroral breakup. *Solid* and *dashed lines* represent average and standard deviation, respectively (Miyashita et al. 2012)



Structure of the Reconnection Region

Figure 11 schematically illustrates the structure of field and flow in the ion-electron decoupling region around the magnetic neutral line. This is a cut by the xz plane and the neutral sheet is the horizontal dashed line in the middle. Although each of the parameters is written in one or two sectors only, overall symmetry is implied. The field parameters are given on the left-hand side, and flow parameters are on the right-hand side.

Ions and electrons enter from top and bottom of the diagram. The flow is the $\mathbf{E} \times \mathbf{B}$ drift under the dawn-to-dusk \mathbf{E}_y prevailing in the magnetosphere. When the plasma comes to a distance of order of the inertia length from the neutral sheet, they can no longer exert the drift motion. (The ion inertia length is 720 km for $n = 0.1 \text{ cm}^{-3}$ and 1,310 km for $n = 0.03 \text{ cm}^{-3}$.) Since this happens further away for ions whose inertia length is about 40 times larger than for electrons, the number flux $\mathbf{F}_{i,z}$ of ions approaching the neutral sheet is much smaller than the flux $\mathbf{F}_{e,z}$ of electrons. Ion-electron decoupling region is produced and a layer of electron excess is formed around the neutral sheet. This results in (1) the electric polarization field \mathbf{E}_z directed toward the neutral sheet and (2) the current system \mathbf{J}_H originating from the electron flow in this layer toward the neutral sheet. The latter is of the nature of the Hall current as it is generated by the difference in the $\mathbf{E}_y \times \mathbf{B}_x$ drift between ions and electrons.

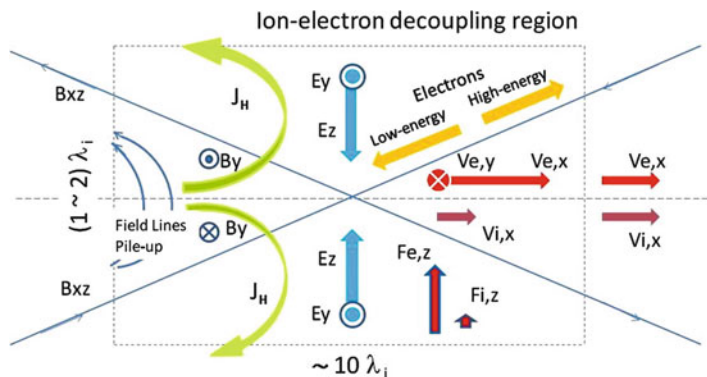


Fig. 11 Overview of the signatures observed in the ion-electron decoupling region around the magnetic neutral line

Accelerated ions and electrons flow away along the neutral sheet. Initially electrons gain much higher speed $V_{e,x}$ than $V_{i,x}$ of ions, and electrons also gain substantial $V_{e,y}$ which is due to the $\mathbf{E} \times \mathbf{B}$ drift under \mathbf{E}_z and \mathbf{B}_x . It takes a distance of several times the ion inertia length before the outflow velocity of electrons is reduced and ions catch up with electrons. In the range where the flow of electrons is being decelerated, the outward velocity of magnetic field lines is also reduced, so that field lines are piled up, that is, the magnetic field is intensified. Energy flux and temperature of the electrons are enhanced around this region, suggesting that electrons are accelerated further by exerting the diamagnetic drift in the direction of $-\mathbf{E}_y$. These enhancements are seen on both earthward and tailward sides of the neutral line but are more pronounced on the earthward side (Imada et al. 2005). Along magnetic field lines, energized electrons (>10 keV) stream outward while low-energy electrons (<5 keV) stream inward. These electron flows carry the Hall current \mathbf{J}_H in and out of the reconnection region since the outflow (inflow) is dominant along field lines closer to (further from) the neutral sheet. The current system of \mathbf{J}_H produces the magnetic field \mathbf{B}_y that makes a quadrupole around the neutral point.

Figure 12 is the average variations in magnetic field and plasma moments constructed from the 30 magnetic reconnection events (Nagai et al. 2013) upon which the above schematic is based. The reconnection region was traversed as it moved tailward past the spacecraft. The vertical line indicates the time when V_x reversed sign, that is, when the neutral line was traversed. From the top, \mathbf{B}_x (panel a) was continually positive showing that the spacecraft stayed on the same side of the neutral sheet. \mathbf{B}_y (panel b) changed from negative to positive representing the quadrupole field due to the Hall current. $V_{\text{perp},x}$ (panel e) of electrons exceeded that of ions just prior to and just after the flow reversal. $V_{\text{perp},y}$ (panel f) of electrons became lower than $-1,100$ km/s at the reversal of V_x . The density (panel g) became $<0.1 \text{ cm}^{-3}$ near the flow reversal, and strong flows of electrons are super-Alfvénic. In most cases, kinetic energy was 0.5–5 keV for the inflowing ions and 13–40 keV for the outflowing ions.

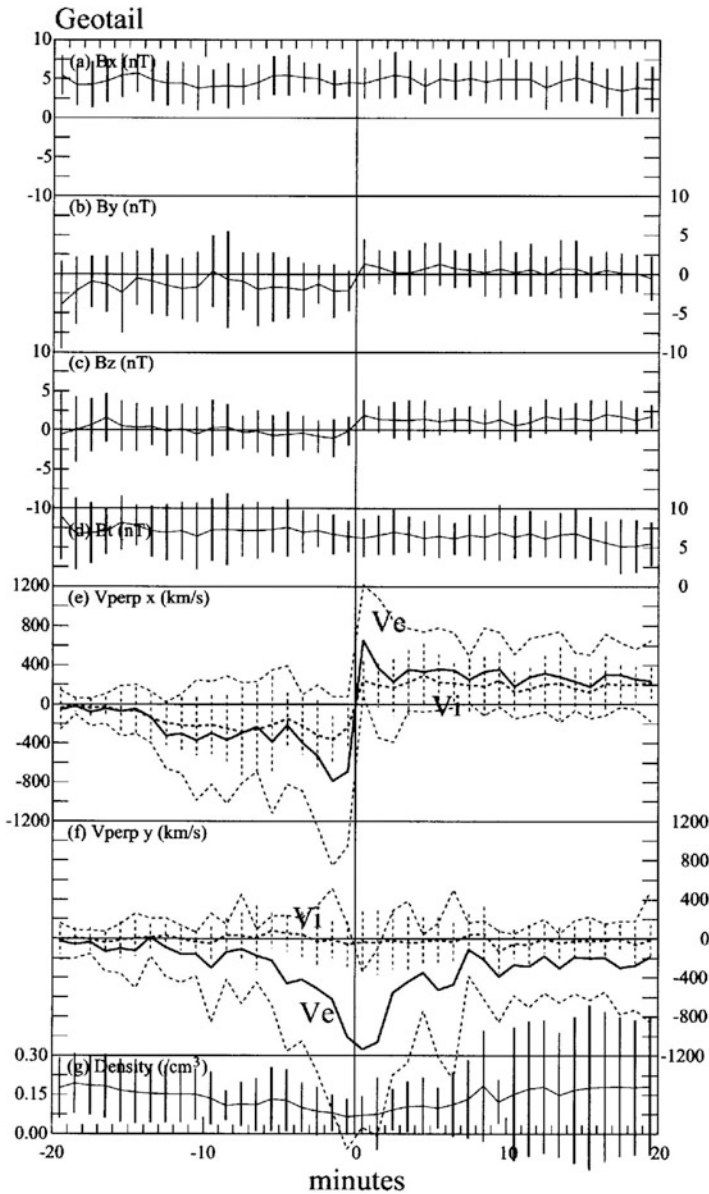


Fig. 12 Observed signatures of magnetic reconnection derived by averaging 30 events. In panels e and f, averages and standard deviations are shown by solid lines and upper/lower envelopes for electrons, and by dashed lines and vertical bars for ions (Nagai et al. 2013)

An example of the ion velocity distribution functions from which the velocities used in Figure 12 were obtained from the velocity distribution functions shown in Figure 13 (Nagai et al. 2013). Panels a and c represent observations on the earthward

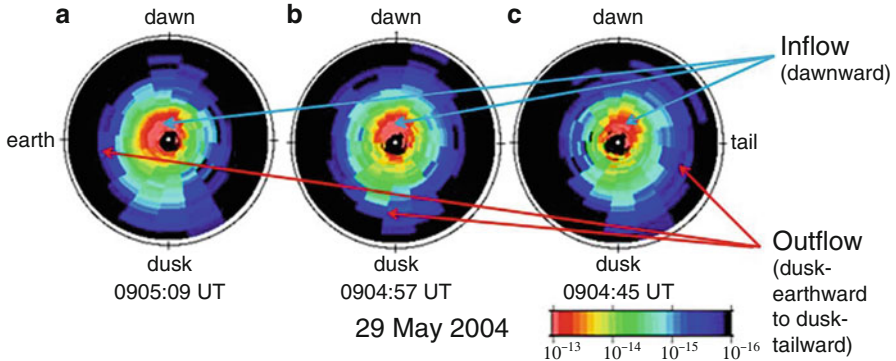


Fig. 13 Velocity distribution functions of ions observed when the neutral line region passed the spacecraft from the tailward side to the earthward side (Nagai et al. 2013)

and tailward sides of the neutral line, respectively. The outer circle corresponds to the ion velocity of 3,000 km/s. Low-energy (incoming toward the neutral sheet region) ions (< 4 keV) were moving downward under the Hall electric field. High-energy (flowing away from the reconnection region) ions (> 10 keV) change their flow direction from earthward (panel a) to tailward (panel c) through duskward (panel b) the across the reconnection region. Their duskward motion can be attributed to the Speiser motion representing half-gyration under weak B_z and skewing of gyration due to non-uniform magnetic field. Ions gain energy through this motion which is in the direction of E_y .

On the earthward side of the NENL position, the thickness of the current at the neutral sheet decreases to less than $\sim 3,000$ km before the onset of reconnection, while on its anti-earthward side, the thinning occurs only after the onset. This suggests that the neutral line forms at or near the anti-earthward edge of the thinned current sheet (Asano et al. 2004). At the start of reconnection, the electric field E_y is enhanced by induction.

Sources of Magnetotail Plasma

Plasmas in the magnetotail originate from either the solar or the terrestrial atmosphere. Plasmas from these sources can be distinguished by their degree of ionization. The plasma from the sun, that is, the solar wind, is almost fully ionized while the plasma from the Earth's atmosphere is mostly singly ionized. The solar plasma enters geomagnetic tubes of force when the field lines of the interplanetary magnetic field (IMF) and of the geomagnetic field are reconnected on the dayside magnetopause, and is carried to the magnetotail across the polar cap. The boundary region of the tail where the solar wind enters is called plasma mantle. In Fig. 14 this supply route, which is dominant, is marked by the arrow 1. The solar wind enters the tail also from the flanks of the magnetotail where turbulent boundary layer is

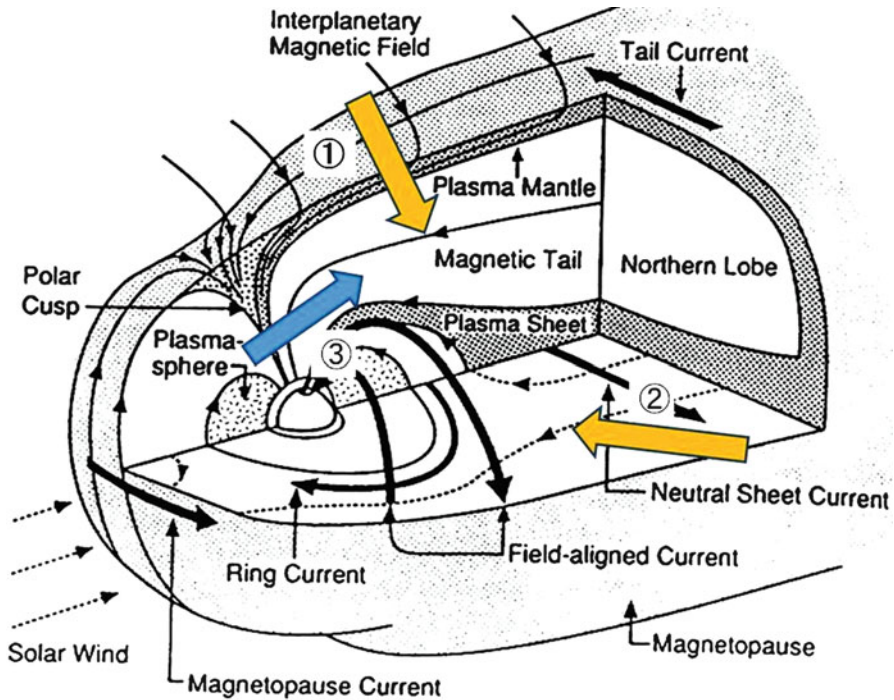


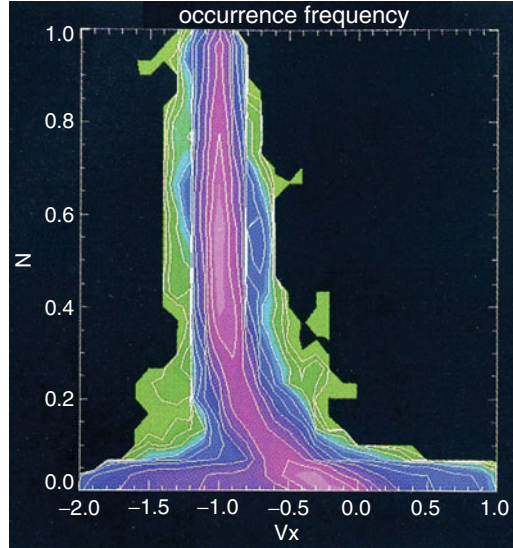
Fig. 14 Supply routes of plasmas to the magnetotail are shown by thick arrows numbered 1–3. Yellow means the solar wind plasma and blue means the terrestrial plasma

formed and plasmas are mixed. This is the route 2. The terrestrial plasma, on the other hand, flows along magnetic field lines from low altitudes making the supply route 3. This plasma originates from the ionosphere but has been accelerated on the way and orders of magnitude more energetic than the pristine plasma in the ionosphere.

Solar Wind Entry Following Magnetic Reconnection on the Dayside Magnetopause

The relation of plasmas in the tail to the solar wind plasma is shown in Fig. 15 where occurrence frequency of density N (normalized to the value in the solar wind) versus velocity V_x (normalized to the absolute magnitude of the solar wind velocity) is shown by color codes where pink (green) represents higher (lower) occurrence frequency. The data obtained at $x < -150 R_E$ were used. The upper portion of the diagram represents the magnetosheath plasma that was flowing with almost the same speed as the solar wind. The lower portion below $N \sim 0.3$, however, represents the tail lobe plasma which has been rarefied and decelerated as they enter deeper in the tail. Then, there is a transition around $N \sim 0.1$ where the velocity

Fig. 15 Relation between density (normalized to solar wind density) and velocity (normalized to the solar wind speed) in the magnetotail. The occurrence frequency is color coded (Maezawa and Hori 1998)



distribution spreads over a broad range extending from about -2.0 to $+1.0$. This can be interpreted to represent the plasma sheet. Cases with positive V_x mean that magnetic reconnection sometimes takes place tailward of the sampling position (Maezawa and Hori 1998).

Although omitted in the model of Fig. 5, shock fronts of the magnetohydrodynamics are developed upstream of the paired field lines that cross the neutral lines. In such instances the plasma sheet boundary corresponds to the shock front. It was found that some of the heated ions escape upstream, and incident ions begin to be heated by them (by way of wave-particle interaction process) in the foreshock region (Saito et al. 1998).

Solar Wind Entry from the Flanks of the Tail

In geomagnetically very quiet times which occur during prolonged periods of the northward IMF, the plasma sheet near dawn and dusk flanks becomes significantly cold and dense, suggesting slow diffusive transport of plasma from the solar wind into the plasma sheet through the magnetotail flanks (Terasawa et al. 1997). Figure 16 shows velocity distribution function of protons observed on such occasions in the dusk region of the tail at $(-14, 22, -4) R_E$. A slice by the **(B, C)** plane, where **B** is magnetic field and **C** is convection velocity, is shown on the left, and the cut of this distribution along the dashed line is on the right. It can be seen in the right panel that “cold and dense” plasma and “hot but tenuous” plasma coexist. The left panel shows that the velocity distribution of cold-dense plasma has bidirectional anisotropy in the **B** direction. The distribution function of electrons (not shown) also shows bidirectional anisotropy. This suggests that the colder but denser plasma

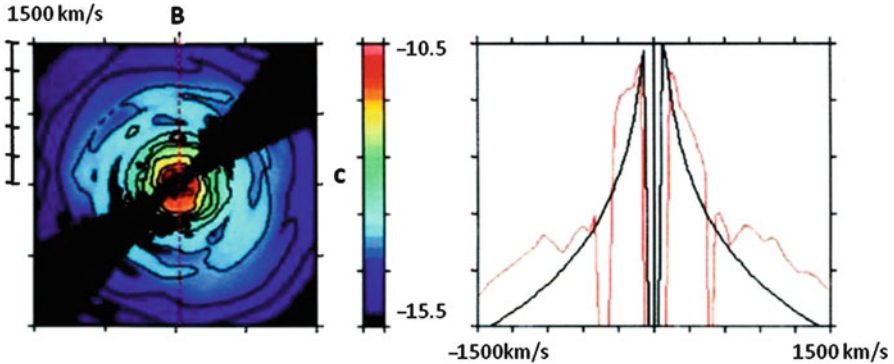


Fig. 16 Coexistence of hot ions and cold ions in the flank region of the magnetotail (Fujimoto et al. 1998)

of the magnetosheath is captured onto the closed field lines of the plasma sheet characterized by hotter but thinner plasma (Fujimoto et al. 1998).

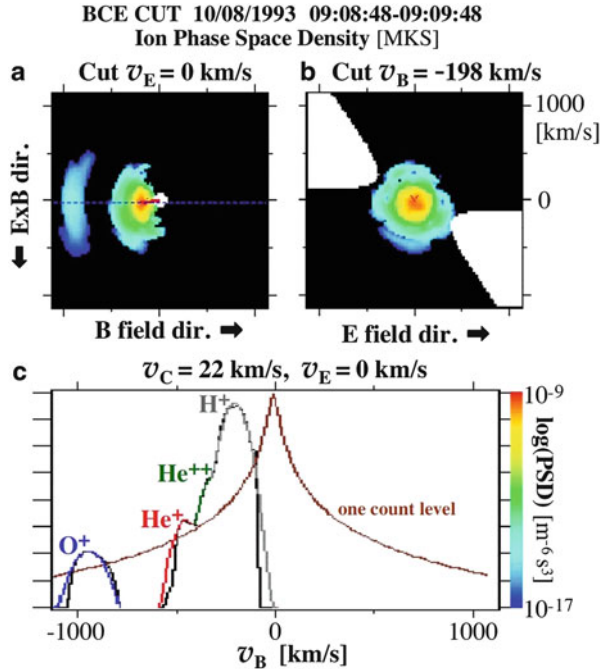
Statistical analysis of these events has revealed the following. Two component protons are frequently seen and are rather stagnant from dusk to midnight. They begin to be seen a few hours after the northward turning of IMF. The thermal energy of the colder component is a few times less than the kinetic energy of the solar wind protons, while that of the hotter component is a few times larger (Nishino et al. 2007).

Kelvin-Helmholtz instability that develops from the velocity shear between the magnetosheath and the magnetospheric plasmas has been considered to play an important role in mixing of the plasmas across the magnetopause. When this instability has grown nonlinearly, a highly rolled-up vortex is formed. In the rolled-up vortex, the tailward speed of a fraction of low-density magnetospheric plasmas exceeds that of the magnetosheath flow. This signature has been found on both dusk and dawn flanks of the tail and is not rare for northward IMF conditions. In all the rolled-up cases, magnetosheath-like ions are detected on the magnetospheric side of the boundary (Hasegawa et al. 2006).

Plasma of the Terrestrial Origin

Plasma that has originated from the Earth's atmosphere is characterized by relative abundance of O^+ and He^+ ions. Figure 17 is an example of such plasma that was observed in the lobe/mantle region of the distant tail at $(x, y, z) = (-141, 6, 2) R_E$ (Seki et al. 1998 and Seki et al. 1999). Panels a and b are contours of the phase space density in the plane of $(\mathbf{B}, \mathbf{E} \times \mathbf{B})$ at $V_E = 0$ and $(\mathbf{E}, \mathbf{E} \times \mathbf{B})$ at $V_B = -198$ km/s, respectively, where $\mathbf{E} \times \mathbf{B}$ ($= \mathbf{C}$) is the direction of convection. It is evident that multiple ion components are present. Panel c is the plot of the phase space density as a function of V_B , namely, the flow speed along magnetic field. This distribution function can be fitted by the sum of multiple shifted Maxwellians

Fig. 17 Coexistence of ions originating from the solar wind (e.g., He^{++}) and from the Earth's atmosphere (e.g., O^+) in the distant tail lobe (Seki et al. 1999)



consisting of He^+ and O^+ as well as H^+ and He^{++} . In these diagrams speeds are scaled by assuming all the ions are protons, but when adjusted for the mass of each constituent, the flow velocities of all ion species turn out to be almost the same, about 200 km/s tailward. For O^+ this means the flow energy of several keV and its density is about 10^{-3} cm^{-3} which is about 1.2 % of the proton component. When projected to an altitude of 1,000 km at latitude of 60° , this yields the outflow flux of $10^8 \text{ cm}^{-2} \text{ s}^{-1}$ of O^+ , which is much higher than the outflow rate of O^+ from the ionosphere. It is also noted that such outflowing ions typically have energies of only 1 keV or less so that their O^+ component would have been swept into the plasma sheet by convection before reaching the distant tail lobe.

Occurrence probability of the ion beams depends on IMF. They tend to be observed in geomagnetically disturbed times that correspond to southward \mathbf{B}_z and in the “loaded quadrant” of the tail which depends on the sign of \mathbf{B}_y of IMF. When geomagnetic field lines are reconnected with IMF having duskward (dawnward) \mathbf{B}_y as well as southward \mathbf{B}_z , resulting open field lines are stretched dawnward (duskward) so that the solar wind plasma is loaded in the dawn (dusk) quadrant of the northern tail mantle. (The opposite is the case for the southern tail mantle.) O^+ ions which originate from the terrestrial atmosphere also show preference for the loaded quadrant. This suggests that the ion beams observed in the tail do not come directly from the polar ionosphere but by way of the outer dayside magnetosphere. When a flux tube containing O^+ is reconnected with IMF on the dayside magnetopause, O^+ will be mixed with the solar wind plasma,

injected toward the high-latitude ionosphere, reflected at mirror points, and finally transported to the “loaded quadrant” of the tail lobe/mantle. This model was tested by comparing the observations in the tail with simultaneous observations by the FAST satellite at low altitudes (1,200–3,400 km), and it was found that phase space densities of locally mirroring O^+ in the high-energy precipitation region on closed field lines are comparable to that of the ion beams in the tail (Seki et al. 2000).

Beam-like O^+ ions at still higher energies around ~ 250 keV have been detected in the distant magnetotail. They occur in geomagnetically disturbed times but are delayed from southward turning of IMF B_z and substorm (Wilken et al. 1998). They were also seen in the magnetosheath adjacent to the magnetopause with an energy dispersion where lower (higher) energy component is found closer to (further from) the magnetopause (Zong and Wilken 1998). These observations also suggest that the leakage of energetic particles of terrestrial origin occurs also from the dayside magnetopause to the magnetosheath.

Waves in the Magnetotail

Because the plasmas in the magnetotail are subject to multitude of sources and acceleration processes while the collision frequencies are very low, their velocity distribution functions can seldom be represented by a single Maxwellian so that they are liable to development of plasma waves. Only a few examples will be described.

Waveform capture (WFC) on board GEOTAIL has revealed that what used to be taken as broadband electrostatic noise in fact represents electrostatic solitary waves (ESW), that is, bipolar potential structures with timescales of 1–50 ms travelling with high velocities along the magnetic field (Matsumoto et al. 1994). They are generated through nonlinear evolution of electron beam instability resulting from the bump-on-tail velocity distribution function of electrons. ESW potential energies are mostly below 4 eV. Observed locations of ESW suggest that such distributions are formed by the electrons streaming away from the neutral lines in both distant and near-Earth regions (Omura et al. 1999).

Low-frequency (1–10 Hz) electromagnetic turbulence is observed in the magnetotail. This can be interpreted to be due to the lower hybrid drift instability (LHDI) driven by the diamagnetic drift of ions. Its contribution to energy dissipation in the magnetic neutral line region would be limited because this mode is stabilized in high β plasma (Shinohara et al. 1998), but it has been suggested that development of LHDI at the edges of current sheet could lead to increase in the number of meandering electrons in a thin current sheet and enhance the growth rate of the tearing mode (Fujimoto et al. 2011).

Saito et al. (2008) have shown that weak variations in B_x in the 0.01–0.02 Hz range that were observed at x of -10 to $-13 R_E$ under high (20–70) β conditions in the vicinity of the magnetic equator are consistent with the ballooning mode. The variation had almost zero frequency in the plasma rest frame which was moving

in the y direction, and the wavelength was of the order of ion Larmor radius. Their paper presented a case where the above observation was made a few minutes before the dipolarization.

Conclusion

GEOTAIL was the first and still is the only spacecraft that explores the magnetotail over the distance of 10–210 R_E from the Earth. When it was in the near-Earth region of the tail, its inclination was optimized for extensive observations in the magnetic neutral sheet region. The science instruments on board were innovative, and most of them are in good shape more than two decades after the launch. The database is made open to the international community and has provided key correlative data in innumerable multispacecraft studies of almost every process taking place in the magnetosphere environment.

On account of the highly sensitive plasma instrument, GEOTAIL has been able to make comprehensive observations of the microscopic (kinetic) structures whose spatial scales are smaller than the ion inertia length. In collisionless plasma such as space plasma, important processes occur in that scale range. Magnetic reconnection is a typical example. Since acceleration of ions takes longer than that of electrons because of larger inertia, ions and electrons are separated in the reconnection region where they are accelerated at the expense of magnetic energy. Other examples were found in the foreshock region upstream of the reconnection region and the low-latitude boundary layer on the flanks of the tail. Observations by GEOTAIL have shed new light on fundamental features of space plasmas.

Advanced understanding gained from *in-situ* observations in the Earth's magnetotail has broad implications on astrophysical and solar phenomena, because collisionless plasmas are prevalent in the universe and magnetic reconnection often plays a key role. Solar X-ray emissions observed by Yohkoh satellite have demonstrated that various dynamic features in solar flares and corona are closely related to magnetic reconnection (e.g., Shibata 1998). XMM-Newton observation of a soft gamma ray repeater is consistent with increasing of the twist of external magnetic field lines during the time leading to the giant flare and decreased twist thereafter brought about by reconnection (Lyutikov 2006). Relativistic winds and jets emanating from neutron stars are also an important domain for the application of reconnection (Kirk 2004). Synchrotron gamma ray flares above 100 MeV in the Crab Nebula observed by Fermi satellite can be modeled by reconnection in the striped wind where electrons can reach high energies before suffering radiation loss (Uzdensky et al. 2011). Theoretical studies of magnetic reconnection and particle acceleration have been extended to relativistic plasma (Zenitani and Hoshino 2007; Hoshino and Lyubarsky 2012).

In fact, LEP on board GEOTAIL contributed to astrophysics already by providing unsaturated γ -ray profile for the first 600 ms of the massive flare from SGR 1806-20, a possible magnetar, which saturated almost all γ -ray detectors.

The implied total energy is comparable to the stored magnetic energy in a magnetar (Terasawa et al. 2005).

GEOTAIL was the first international mission in the field of magnetospheric physics where US and Japanese scientists/engineers worked together as a joint team. Interpersonal relationships developed through close and continuous interactions throughout the program at the working level and played an important role in “translating the untranslatable” whenever things got complicated. The development of a mutual trust relationship between the partners was perhaps the most critical element of all for success (Acuña 1999). The lessons learned will serve as a valuable guide in international efforts for planetary defense.

References

- Acuña MH (1999) International cooperation with Japan in the international solar-terrestrial physics/GGS program. In: U.S.-European-Japanese workshop on space cooperation, National Academy Press, Washington, DC, pp 28–32
- Asano Y, Mukai T, Hoshino M, Saito Y, Hayakawa H, Nagai T (2004) Statistical study of thin current sheet evolution around substorm onset. *J Geophys Res* 109:A05213
- Fairfield DH, Mukai T, Brittnacher M, Reeves GD, Kokubun S, Parks GK, Nagai T, Matsumoto H, Hashimoto K, Gurnett DA, Yamamoto T (1999) Earthward flow bursts in the inner magnetotail and their relation to auroral brightening, AKR intensifications, geosynchronous particle injection and magnetic activity. *J Geophys Res* 104:355–370
- Fujimoto M, Terasawa T, Mukai T, Saito Y, Yamamoto T, Kokubun S (1998) Plasma entry from the flanks of the near-Earth magnetotail: geotail observations. *J Geophys Res* 103:4391–4408
- Fujimoto M, Shinohara I, Kojima H (2011) Reconnection and waves: a review with a perspective. *Space Sci Rev* 160:123–143
- Hasegawa H, Fujimoto M, Takagi K, Saito Y, Mukai T, Reme H (2006) Single-spacecraft detection of rolled-up Kelvin-Helmholtz vortices at the flank magnetopause. *J Geophys Res* 111:A9023
- Hones EW Jr (1984) Plasma sheet behavior during substorms. In: Hones EW Jr (ed) *Magnetic reconnection in space and laboratory plasmas*. American Geophysical Union, Washington, DC, pp 178–184
- Hoshino M, Lyubarsky Y (2012) Relativistic reconnection and particle acceleration. *Space Sci Rev* 173:521–533
- Ieda A, Machida S, Mukai T, Saito Y, Yamamoto T, Nishida A, Terasawa T, Kokubun S (1998) Statistical analysis of the plasmoid evolution with Geotail observations. *J Geophys Res* 103:4453–4465
- Ieda A, Fairfield DH, Mukai T, Saito Y, Kokubun S, Liou K, Meng CI, Parks GK, Brittnacher MJ (2001) Plasmoid ejection and auroral brightening. *J Geophys Res* 106:3845–3857
- Ieda A, Fairfield DH, Slavin JA, Liou K, Meng CI, Machida S, Miyashita Y, Mukai T, Nose M, Shue JH, Parks GK, Fillingim MO (2008) Longitudinal association between magnetotail reconnection and auroral breakup based on Geotail and Polar observations. *J Geophys Res* 113:A08207
- Imada S, Hoshino M, Mukai T (2005) Average profiles of energetic and thermal electrons in the magnetic reconnection regions. *Geophys Res Lett* 32:L09101
- Kirk JG (2004) Particle acceleration in relativistic current sheets. *Phys Rev Lett* 92:181101
- Lytikov M (2006) Magnetar giant flares and afterglows as relativistic magnetized explosions. *Mon Not R Astron Soc* 367:1594–1602
- Maezawa K, Hori T (1998) The distant magnetotail: Its structure, IMF dependence, and thermal properties. In: Nishida A, Baker DN, Cowley SWH (eds) *New perspectives on the Earth’s magnetotail*. American Geophysical Union, Washington, DC, pp 1–19

- Matsumoto H, Kojima H, Miyatake T, Omura Y, Okada M, Nagano I, Tsutui M (1994) Electrostatic solitary waves (ESW) in the magnetotail: BEN wave forms observed by GEOTAIL. *Geophys Res Lett* 21:2915–2918
- McFadden LP et al (including Mukai T, Saito Y) (2007) In-flight calibration and performance verification. In West W, Evance DS, von Steiger R (eds) ISSI Scientific Report SR-007
- Miyashita Y, Machida S, Nose M, Liou K, Saito Y, Paterson WR (2012) A statistical study of energy release and transport midway between the magnetic reconnection and initial dipolarization regions in the near-Earth magnetotail associated with substorm expansion onsets. *J Geophys Res* 117:A11214
- Nagai T, Fujimoto M, Saito Y, Machida S, Terasawa T, Nakamura R, Yamamoto T, Mukai T, Nishida A, Kokubun S (1998) Structure and dynamics of magnetic reconnection for substorm onsets with Geotail observation. *J Geophys Res* 103:4419–4440
- Nagai T, Fujimoto M, Nakamura R, Baumjohann W, Ieda A, Shinohara I, Machida S, Saito Y, Mukai T (2005) Solar wind control of the radial distance of the magnetic reconnection site in the magnetotail. *J Geophys Res* 110:A09208
- Nagai T, Shinohara I, Zenitani S, Nakamura R, Nakamura TKM, Fujimoto M, Saito Y, Mukai T (2013) Three-dimensional structure of magnetic reconnection in the magnetotail from Geotail observations. *J Geophys Res* 118:1667–1678
- Nakamura R, Baumjohann W, Schoedel R, Brittnacher M, Sergeev VA, Kubyskhina M, Mukai T, Liou K (2001) Earthward flow bursts, auroral streamers, and small expansions. *J Geophys Res* 106:10,791–10,802
- Nishida A, Mukai T, Yamamoto T, Saito Y, Kokubun S (1996) Magnetospheric convection in geomagnetically active times, 1. Distance to neutral lines. *J Geomag Geoelectr* 48:489–501
- Nishida A (1994) The Geotail mission. *Geophys Res Lett* 25:2871–2873
- Nishino MN, Fujimoto M, Ueno G, Maezawa K, Mukai T, Saito Y (2007) Geotail observations of two-component protons in the midnight plasma sheet. *Ann Geophys* 25:2229–2245
- Omura Y, Kojima H, Miki N, Matsumoto H (1999) Two-dimensional electrostatic solitary waves observed by GEOTAIL in the magnetotail. *Adv Space Res* 24:55–58
- Pontius DH, Wolf RA (1990) Transient flux tubes in the terrestrial magnetosphere. *Geophys Res Lett* 17:49–52
- Saito Y, Mukai T (2007) The method of calculating absolutely calibrated ion and electron velocity moments, ISAS Research Note No. 815, JAXA
- Saito Y, Mukai T, Terasawa T (1998) Kinetic structure of the slow-mode shocks in the Earth's magnetotail. In: Nishida A, Baker DN, Cowley SWH (eds) *New perspectives on the Earth's magnetotail*. American Geophysical Union, Washington, DC, pp 103–115
- Saito MH, Miyashita Y, Fujimoto M, Shinohara I, Saito Y, Liou K, Mukai T (2008) Ballooning mode waves prior to substorm-associated dipolarizations: Geotail observations. *Geophys Res Lett* 35:L07103
- Seki K, Hirahara M, Terasawa T, Mukai T, Saito Y, Machida S, Yamamoto T, Kokubun S (1998) Statistical properties and possible supply mechanisms of tailward cold O^+ beams in the lobe/mantle regions. *J Geophys Res* 103:4477–4489
- Seki K, Hirahara M, Terasawa T, Mukai T, Kokubun S (1999) Properties of He^+ beams observed by Geotail in the lobe/mantle regions: comparison with O^+ beams. *J Geophys Res* 104:6973–6985
- Seki K, Elphic RC, Thomsen MF, Bonnel J, Lund EJ, Hirahara M, Terasawa T, Mukai T (2000) Cold flowing O^+ beams in the lobe/mantle at Geotail: does FAST observe the source? *J Geophys Res* 105:15931–15944
- Sergeev VA, Sauvaud JA, Popescu D, Kovrazhkin RA, Liou K, Newell PT, Brittnacher M, Nakamura R, Mukai T, Reeves GD (2000) Multi-spacecraft observation of a narrow transient plasma jet in the Earth's plasma sheet. *Geophys Res Lett* 27:851–854
- Shibata K (1998) Evidence of magnetic reconnection in solar flares and a unified model of flares. *Astrophys Space Sci* 264:129–144

- Shinohara I, Nagai T, Fujimoto M, Terasawa T, Mukai T, Tsuruda K, Yamamoto T (1998) Low-frequency electromagnetic turbulence observed near the substorm onset site. *J Geophys Res* 103:20365–20388
- Terasawa T, Fujimoto M, Mukai T, Shinohara I, Saito Y, Yamamoto T, Machida S, Kokubun S, Lazarus AJ, Steiberg JT, Lepping RP (1997) Solar wind control of density and temperature in the near-Earth plasma sheet: WIND-GEOTAIL collaboration. *Geophys Res Lett* 24:935–938
- Terasawa T, Tanaka YT, Takei T, Kawai N, Yoshida A, Nomoto K, Yoshikawa I, Saito Y, Kasaba Y, Takashima T, Mukai T, Noda H, Murakami T, Watanabe K, Muraki Y, Yokoyama T, Hoshino M (2005) Repeated injections of energy in the first 600 ms of the giant flare of SGR 1806-20. *Nature* 434:1010–1111
- Uzdensky DA, Cerutti B, Begelman MC (2011) Reconnection-powered linear accelerator and gamma-ray flares in the Crab Nebula. *Astrophys J Lett* 737:L40
- Wilken B, Zong QG, Doke T, Mukai T, Yamamoto T, Reeves GD, Maezawa K, Kokubun S, Ullaland S (1998) Substorm activity on January 11, 1994: Geotail observations in the distant tail during the leading phase of a corotation region. *J Geophys Res* 103:17671–17689
- Zenitani S, Hoshino M (2007) Particle acceleration and magnetic dissipation in relativistic current sheet of pair plasmas. *Astrophys J* 670:702–726
- Zong QG, Wilken B (1998) Layered structure of energetic oxygen ions in the dayside magnetosheath. *J Geophys Res* 25:4121–4124